



Stress-induced high- T_c superconductivity in solid molecular hydrogen

Xianqi Song^{a,b,1}, Chang Liu^{a,b,c,d,1}, Quan Li^{a,b,c,d,2}, Russell J. Hemley^{e,2}, Yanming Ma^{a,b,c,2}, and Changfeng Chen^{f,2}

Edited by David Ceperley, University of Illinois at Urbana–Champaign, Urbana, IL; received December 17, 2021; accepted April 29, 2022

Solid molecular hydrogen has been predicted to be metallic and high-temperature superconducting at ultrahigh hydrostatic pressures that push current experimental limits. Meanwhile, little is known about the influence of nonhydrostatic conditions on its electronic properties at extreme pressures where anisotropic stresses are inevitably present and may also be intentionally introduced. Here we show by first-principles calculations that solid molecular hydrogen compressed to multimegabar pressures can sustain large anisotropic compressive or shear stresses that, in turn, cause major crystal symmetry reduction and charge redistribution that accelerate bandgap closure and promote superconductivity relative to pure hydrostatic compression. Our findings highlight a hitherto largely unexplored mechanism for creating superconducting dense hydrogen, with implications for exploring similar phenomena in hydrogen-rich compounds and other molecular crystals.

high pressure | anisotropic stresses | metallic hydrogen | superconductivity | first-principles calculations

Since Wigner and Huntington's (1) pioneering work, pressure-induced metallization of hydrogen has attracted immense interest and impelled advances in theoretical and computational methods, ultrahigh-pressure devices, and related measurement and characterization techniques (2, 3). The prediction (4) that metallic hydrogen may be a high-temperature superconductor driven by the Bardeen-Cooper-Schrieffer (BCS)-type phonon-mediated mechanism further invigorated the study of this fascinating material and its enigmatic properties. As a prominent thermodynamic quantity, pressure, which is defined as hydrostatic, drives the formation of new material phases through structural transitions and electronic bandgap closure (5). Two main avenues have been pursued for producing metallic hydrogen at high pressure: 1) closure of the electronic bandgap of solid molecular hydrogen and 2) dissociation of hydrogen molecules to form monatomic metal. These mechanisms have been explored through optical and electrical conductivity techniques over the years (6–16). In addition, at least five molecular phases, labeled I to V, have been documented experimentally to pressures up to 400 GPa and temperatures up to 300 K (17–21). These very high static pressures can significantly limit, constrain, and challenge full experimental characterization of materials, especially above 300 GPa, leading to ambiguities and controversies in the interpretation of reported results.

Theoretical studies (22–27) of the metallization of solid hydrogen have focused on its formation under hydrostatic pressure. However, conditions inside diamond anvil cells (DACs) at the required pressures (e.g., >300 GPa) can introduce nonuniform deformations and anisotropic stresses in the vicinity of the sample as revealed by direct X-ray imaging study above 300 GPa (28). More recent studies have further explored these effects (29, 30) and have also unveiled unprecedented structural ductility in diamond under large multiaxial deformation modes (31, 32), underscoring complex strain conditions inside DACs under extreme loading conditions. It is therefore instructive to establish the influence of anisotropic stresses on the evolution of structural and electronic properties of molecular hydrogen under nonhydrostatic pressure conditions (more discussion of nonhydrostatic stress states in DACs can be found in *SI Appendix*). Although gases that are solidified under pressure are often assumed to be hydrostatic over a range of pressures, direct measurements indicate the development of anisotropic strains even well below 100 GPa (33). Moreover, significant pressure gradients were documented even in the earliest optical studies of closing of the bandgap above 200 GPa (2, 7).

Here we report an exploratory study of metallization and superconductivity of solid molecular hydrogen under anisotropic stresses, i.e., at nonhydrostatic pressures. Our first-principles stress-strain calculations establish that despite being a soft and plastic crystal at low pressures (and temperatures), solid hydrogen at megabar pressures can sustain considerable uniaxial compressive and shear stresses, and such anisotropic stresses can have a major impact on physical properties. Prominent effects include lattice symmetry

Significance

Metallic hydrogen has long been considered the Holy Grail of high-pressure physics that holds the intriguing possibility of realizing room-temperature superconductivity. However, the ultrahigh pressures required for hydrogen metallization impose severe experimental challenges and constraints on synthesis and characterization, leaving large ambiguities and controversies in the interpretation of reported results. We show that nonhydrostatic stresses offer a viable route to promote metallization and superconductivity in hydrogen at more accessible static compression conditions (e.g., <300 GPa). Such stress anisotropy is expected to be highly dependent on sample and measurement conditions, which may explain the discrepancies in previously reported experimental results, including variations in the rate of bandgap closure and onset of electrical conductivity in solid molecular hydrogen.

The authors declare no competing interest.

This article is a PNAS Direct Submission.

Copyright © 2022 the Author(s). Published by PNAS. This article is distributed under [Creative Commons Attribution-NonCommercial-NoDerivatives License 4.0 \(CC BY-NC-ND\)](#).

¹X.S. and C.L. contributed equally to this work.

²To whom correspondence may be addressed. Email: liquan777@jlu.edu.cn, rhemley@uic.edu, mym@jlu.edu.cn, or changfeng.chen@univ.edu.

This article contains supporting information online at <https://www.pnas.org/lookup/suppl/doi:10.1073/pnas.2122691119/-DCSupplemental>.

Published June 24, 2022.

reduction and ensuing changes in the electronic band structure that accelerate the bandgap closure, leading to metallization, and enhance the electron–phonon coupling (EPC), giving rise to superconductivity. In particular, we find that shear deformations are highly effective in inducing metallic and superconducting states at much reduced hydrostatic pressures. These phenomena are driven by robust underpinning mechanisms and are therefore expected to remain intact when possible corrections by thermal and quantum effects are further considered. The present findings may explain loading-dependent differences in reported experimental results (9–16, 34, 35) and show that introducing controlled nonhydrostatic stresses is a viable route to promote metallization and superconductivity in hydrogen at readily accessible static compression conditions (e.g., <300 GPa).

Stress Responses and Bandgap Evolution of Solid Molecular Hydrogen. To explore the impact of anisotropic stresses on the transition of solid hydrogen from insulating to metallic and potentially high- T_c superconducting states, we focus on phase III of solid hydrogen, which was discovered in 1988 (2, 6) and has been predicted and observed to be the stable insulating phase at temperatures below 200 K in the pressure range of about 150 to 400 GPa before potentially turning metallic upon further compression. The extremely high pressures required to achieve metallization have been a formidable challenge to reliable measurements and analysis. Theoretical calculations (17, 36) for phase III have predicted two nearly degenerate and thus coexisting structures of $C2/c$ symmetry containing 12 and 24 atoms per unit cell, respectively, which are compatible with the low-temperature Raman and infrared (IR) spectra (36). In this work, we focus on the $C2/c$ -12 structure (Fig. 1 *A* and *B*) as an exemplary case study; our studies show that this phase is able to sustain large anisotropic stresses and more easily transform into metallic states. We first performed extensive first-principles calculations to determine the stress responses of the $C2/c$ structure to anisotropic compression and shear strains in the hydrostatic pressure range of 200 to 350 GPa, and key representative stress responses are summarized in Fig. 1 *C* and *D* (full stress–strain relations are given in *SI Appendix*, Figs. S1 and S2 and crystal structure information of representative deformed molecular hydrogen is listed in *SI Appendix*, Table S1). It is seen that the structure can sustain considerable anisotropic compressive stresses ranging from 30 to 60 GPa that increase with rising hydrostatic pressure of 200 to 350 GPa or shear stresses of about 30 GPa that are insensitive to hydrostatic pressure.

Electronic band-structure calculations show that these nonhydrostatic stresses that give rise to anisotropic strains lower the bandgap E_g relative to the equivalent isotropic stresses or hydrostatic pressures (*SI Appendix*, Fig. S3) as shown in Fig. 1 *E* and *F*, stemming from band shifts and splittings caused by the symmetry reduction of the deformed crystal. In particular, we find that shear strains ε_{xx} are highly effective in reducing E_g ; for instance, a shear stress $\sigma_{xx} = 20$ GPa at $\varepsilon_{xx} = 0.06$ along the (010)[001] direction reduces E_g at hydrostatic pressure of 200 GPa to approximately E_g at 250 GPa. Remarkably, a shear stress $\sigma_{xx} = 33$ GPa along the (001)[010] direction causes a complete bandgap closure at 250 GPa (Fig. 1*E*), which occurs at 370 GPa under hydrostatic conditions. At higher pressures, bandgap closure occurs at smaller shear strains, as shown in Fig. 1*E* for selected cases (see *SI Appendix*, Fig. S1 for more comprehensive results).

We also examine the evolution of E_g with excess uniaxial compressive strain (ε_{zz}) added to compressive strains induced by hydrostatic pressure. The results show a reduction of E_g at

the rate of about 20 meV/GPa ($\Delta E_g/\Delta\sigma_{zz} = 0.9$ eV/45 GPa), which is greater than 16 meV/GPa ($\Delta E_g/\Delta P = 2.4$ eV/150 GPa) of E_g reduction under hydrostatic pressure (Fig. 1 *D* and *F*). The metallization can be realized at 350 GPa by introducing an additional normal compressive stress of about 23 GPa. Additional results on the compressive stress–strain and corresponding E_g –strain relations presented in *SI Appendix*, Fig. S2 indicate that anisotropic compressive stresses can also play a role but are less effective compared with shear stresses in inducing the metallization.

The stress distribution of samples in DACs at multimegabar pressures can be highly complex. Experimental studies show that samples can be significantly deformed under such loading, resulting in both cupping of the anvils and flow of the gasket around the sample in response to differences in elasticity, strength, and plasticity of the anvil, sample, and gasket material (7, 28, 29). Indeed, the true stress states of such samples are in general triaxial and can depart from the biaxial symmetry of ideal compression of a symmetrical disk-shaped sample surrounded by gasket and anvils. In addition to this complexity in the true stress states, there is a lack of information about crystal orientations and texture of the polycrystal samples. Moreover, the crystal structure considered here has relatively low symmetry. Given the above, the effects of uniaxial compressive stress and shear stress are used here as perturbations to the pure hydrostatic pressures that have been considered in all previous theoretical work on highly compressed hydrogen.

We calculated stresses and bandgap variations associated with uniaxial strains along [100], [010], and [001] for a single crystal of $C2/c$ structured molecular hydrogen. The results show that the stress and bandgap variations are insensitive to the direction of the uniaxial stress (*SI Appendix*, Fig. S2). At 350 GPa, for example, where metallization occurs under uniaxial stress in all three directions, the stress and bandgap responses in the [010] and [001] directions are nearly degenerate with those in the [100] direction, with bandgap closure occurring at a slightly (1%) lower strain in the [100] direction. Moreover, all real samples deform to some degree at these conditions, thereby giving rise to potentially significant anisotropic stresses as discussed above. In this first attempt to explore how the anisotropic stress conditions affect the properties of hydrogen at static multimegabar DAC loading conditions, we find that the uniaxial compression has a small effect, even under the most favorable [100] case, compared to that of shear strains in inducing bandgap closure and metallization in the $C2/c$ phase of solid molecular hydrogen.

Shear-Induced Metallization of Molecular Hydrogen. To further elucidate the appreciable modifications of electronic properties in nonhydrostatic environments, we performed a quantum theory of atoms in molecules (QTAIM) analysis of changes of charge states in response to stress-induced structural variations. We examine the bonding structures and charge density at bond critical points (BCPs) to evaluate the bonding strength and charge transfer. When hydrostatic pressure increases from 250 to 300 GPa, the charge density values at the BCPs of the hydrogen molecules remain unchanged (2.07 to 2.07 and 2.12 to 2.12) and the values between hydrogen molecules rise by about 0.08 a.u. (0.62 to 0.70, 0.61 to 0.69, and 0.59 to 0.67) (see *SI Appendix*, Fig. S4 for more details), implying almost constant bond length of H_2 molecules and increased intermolecular interactions, producing pressure-induced energy-band broadening and E_g decrease (Fig. 2 *C* and *D*). Shear deformation drives intramolecular charge delocalization and differential evolution of hydrogen atomic distance (*SI Appendix*, Fig. S5 *A* and *B*) while enhancing intermolecular

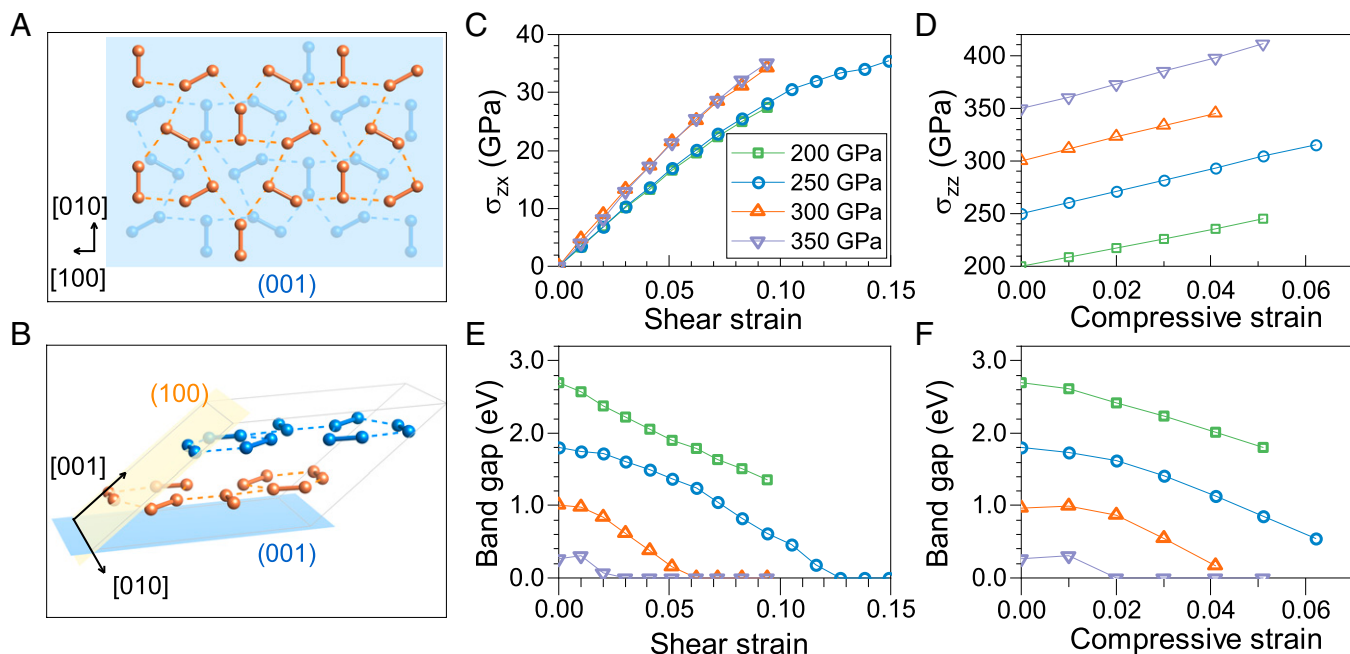


Fig. 1. Structure and stress and bandgap responses of solid molecular hydrogen to anisotropic stresses. (A and B) Top (A) and polyhedral (B) views of the $C2/c$ phase. The thick solid lines represent the intramolecular covalent bonds of H_2 and the thin dashed lines are intermolecular links. The light gray lines outline the unit cell. (C) First-principles-determined stable stress responses to shear strains along the (010)[001] direction (the loading path with the steepest descent of E_g) at hydrostatic pressures of 200, 300, and 350 GPa and along the (001)[010] direction (the loading path with the easiest metallization of E_g) at 250 GPa. (D) First-principles-determined stable stress responses to compressive strains in the [100] direction at 200, 250, 300, and 350 GPa. (E and F) Shear and compressive strain-modified E_g along the above selected loading paths.

interactions and breaks the degeneracy of electronic states due to symmetry reduction. The change of charge density at BCPs of the $C2/c$ structure under combined hydrostatic pressure of 250

GPa and shear stress of $\sigma_{zx} = 35$ GPa ($\varepsilon_{zx} = 0.149$) in the (001)[010] direction (Fig. 2A) shows an in-plane charge transfer from intramolecular to intermolecular regions (the distance of

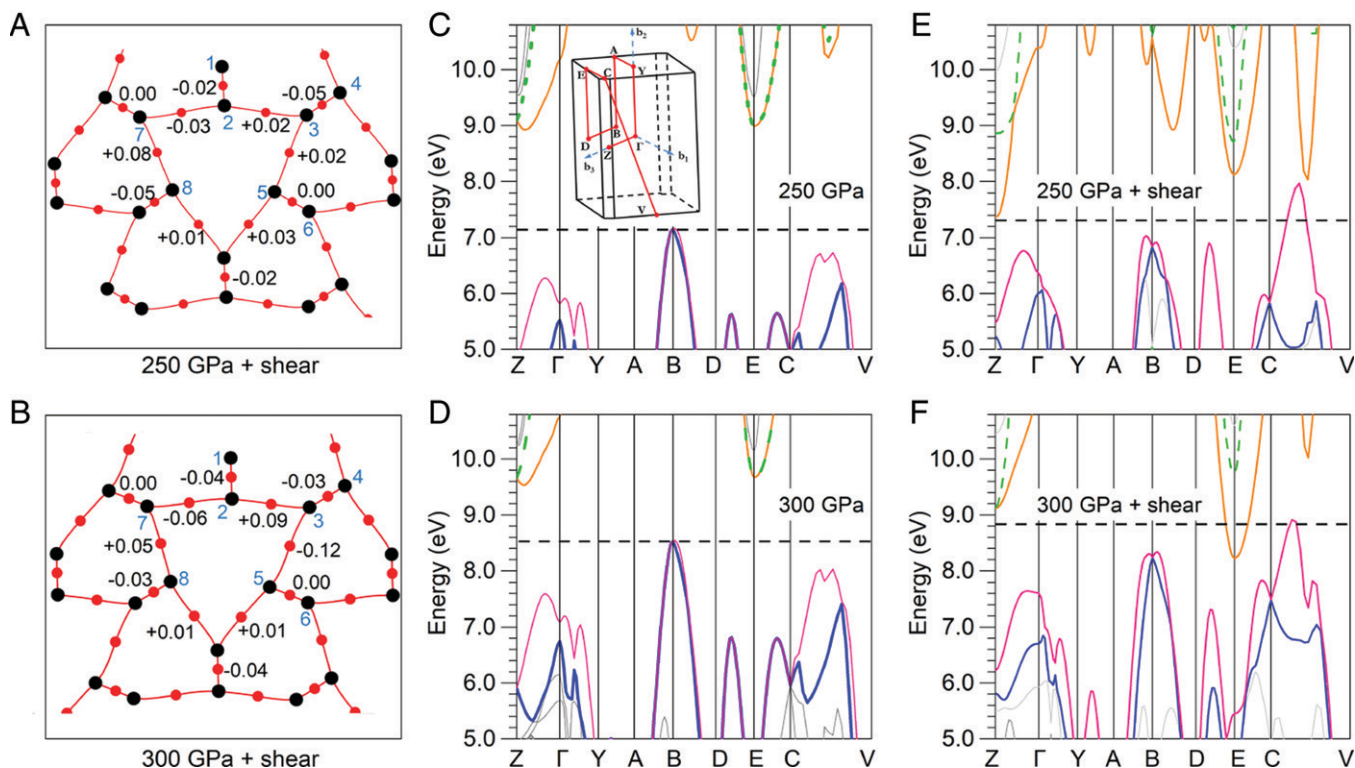


Fig. 2. Electronic properties of shear-deformed $C2/c$ hydrogen. (A and B) QTAIM analysis of charge states in the (001) plane of shear-deformed $C2/c$ -based structure at 250 and 300 GPa. The large (small) black (red) spheres represent hydrogen atoms and BCPs, respectively. The change of charge density for BCPs is given in the atom unit. (C and D) Electronic band structures at the hydrostatic pressure of 250 and 300 GPa. Inset shows the Brillouin zone path for calculating the band structures. (E and F) Electronic band structures of shear-deformed $C2/c$ -based structure at $\sigma_{zx} = 35$ GPa ($\varepsilon_{zx} = 0.149$) in the (001)[010] direction at 250 GPa and at $\sigma_{zx} = 34$ GPa ($\varepsilon_{zx} = 0.094$) in the (010)[001] direction at 300 GPa. The black dashed lines mark the Fermi energy. The bands are colored to exhibit band shifts and splits.

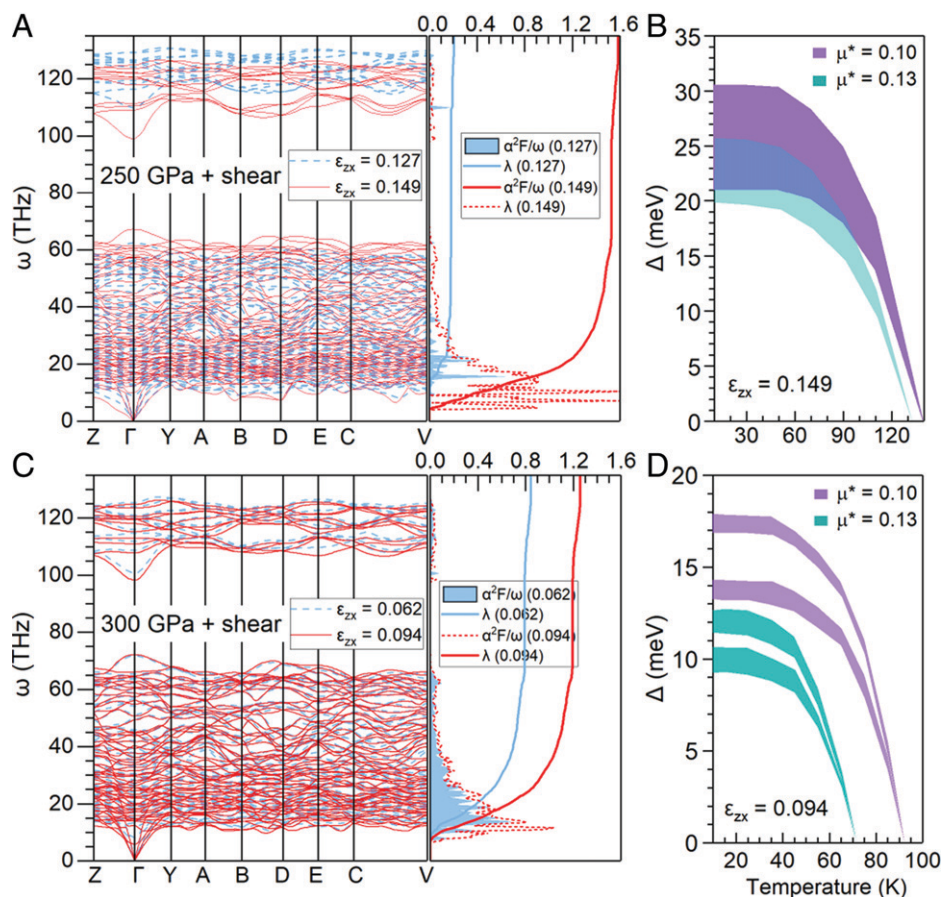


Fig. 3. Shear-induced superconductivity in C2/c hydrogen. (A and B) Phonon dispersion relations $\omega(k)$ and Eliashberg spectral function $\alpha^2F(\omega)/\omega$ and $\lambda(\omega)$ at $\sigma_{zx} = 33$ GPa ($\epsilon_{zx} = 0.127$) and $\sigma_{zx} = 35$ GPa ($\epsilon_{zx} = 0.149$) (A) and the anisotropic superconducting gap (Δ) and superconducting critical temperatures (T_c) at shear strain $\epsilon_{zx} = 0.149$ in the (001)[010] direction (B) at 250 GPa. (C and D) Phonon dispersion relations $\omega(k)$ and Eliashberg spectral function $\alpha^2F(\omega)/\omega$ and $\lambda(\omega)$ at $\sigma_{zx} = 25$ GPa ($\epsilon_{zx} = 0.062$) and $\sigma_{zx} = 34$ GPa ($\epsilon_{zx} = 0.094$) (C) and the anisotropic superconducting gap (Δ) and T_c at shear strain $\epsilon_{zx} = 0.094$ in the (010)[001] direction (D) at 300 GPa.

H7 to H8 from 1.190 to 1.134 Å and H3 to H5 from 1.190 to 1.171 Å), weakening the intramolecular bonds, elongating the H₂ units, and resulting in hole-type bands (Fig. 2E). Meanwhile, shear deformation causes the growth of charge distribution in the interlayer region under shear strains in the (010)[001] direction at 300 GPa (Fig. 2B) with decreasing interlayer spacing (the distance of H3 to H5 from 1.145 to 1.260 Å). The antibonding states of H₂ molecules start to be filled, lowering the conduction band minimum, producing the electron-type band crossing at the Fermi energy, and mediating an indirect band gap closure (Fig. 2F).

Superconductivity in Shear-Deformed Molecular Hydrogen.

There have been extensive theoretical studies of potentially very high- T_c superconductivity in molecular hydrogen induced by hydrostatic compression (37–39). The present work expands such studies by introducing additional tuning mechanisms via anisotropic stresses, which drives metallization of the molecular solid at considerably reduced pressures. We further examine superconductivity of solid molecular hydrogen under shear strains along the easiest metallization paths in the (001)[010] direction at 250 GPa and the (010)[001] direction at 300 GPa. We find enhanced electron–phonon coupling under shear strains. To expose the underlying mechanism, we have calculated the phonon dispersion relations and the Eliashberg spectral function (Fig. 3). Major contributions to the electron–phonon coupling parameter λ come from the low-frequency branches (acoustic phonons and librations) around 10 to 20 THz corresponding to the translational and rotational motions of the H₂ molecules.

The phonons characterize the centers-of-mass molecular motions and the librations correspond to coupled restricted rotations (40). The distinguishable high-frequency vibrons are coupled stretchy vibrations of the H₂ molecules; notably these give rise to large peaks in the Eliashberg spectral function $\alpha^2F(\omega)$ at some q points but the high phonon frequency ω limits their contributions to the electron–phonon coupling parameter. For the (001)[010] shear loading path at 250 GPa, the in-plane charge transfers from the intramolecular to intermolecular regions, which weakens the covalent diatomic molecular bonds and softens the vibrons, reducing the intermolecular repulsion and softening the librations (Fig. 3A). Meanwhile, the hole-type band crosses the Fermi energy along the Brillouin zone path C \rightarrow V (SI Appendix, Fig. S6 A and B), producing superconducting critical temperatures (T_c) of 132 K ($\mu^* = 0.13$) to 140 K ($\mu^* = 0.10$) at shear strain $\epsilon_{zx} = 0.149$ (Fig. 3B). For the (010)[001] shear loading path at 300 GPa, the incremental accumulation of interlayer electrons with rising strains contributes to the electron–phonon coupling at $\epsilon_{zx} = 0.094$ by initiating new topologies of the Fermi surface (SI Appendix, Fig. S6 C and D) and softening phonons (Fig. 3C). The change produces a two-gap superconducting state stemming from the anisotropic and varied Fermi surface structures with a T_c of 72 K ($\mu^* = 0.13$) to 93 K ($\mu^* = 0.10$) (Fig. 3D).

Molecular Hydrogen under Anisotropic Compressive Strains.

We also examined C2/c hydrogen under anisotropic compressive strains at 350 GPa (Fig. 4). The degeneracy of the conduction

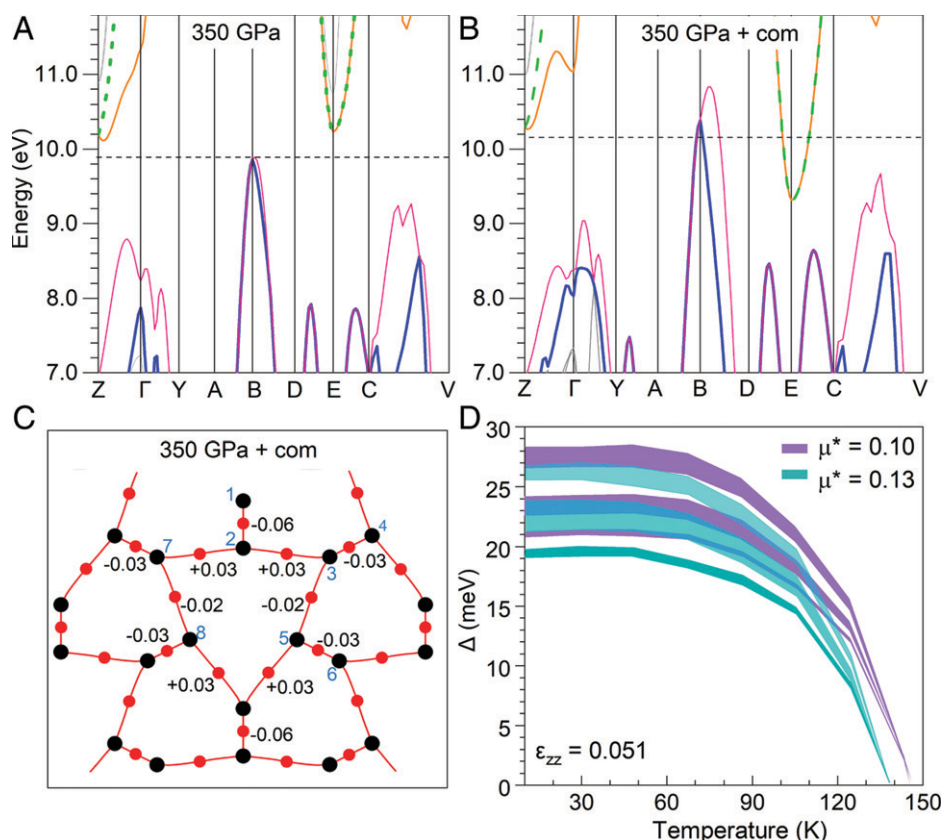


Fig. 4. Electronic properties of C2/c hydrogen under anisotropic strain at 350 GPa. (A and B) Electronic band structures at 350 GPa and at $\sigma_{xx} = \sigma_{yy} = 350$ GPa, $\sigma_{zz} = 411$ GPa ($\varepsilon_{zz} = 0.051$) in the [100] direction. The black dashed lines mark the Fermi energy. The bands are colored to exhibit band shifts and splits. (C) The structure and charge density based on QAIM analysis of C2/c hydrogen under conditions in B. (D) The corresponding superconducting gap (Δ) and T_c .

band remains intact, but the conduction band minimum drops as in the shear-deformed cases (Fig. 4 A and B). In contrast to the hydrostatic and shear-strain cases, the bond lengths of the hydrogen molecules increase here (SI Appendix, Fig. S5C), indicating more intramolecular electron transfer to the intermolecular (in-plane and interlayer) regions, in agreement with the charge density analysis of BCPs from QAIM (Fig. 4C). These new charge states produce complex band characteristics and Fermi surfaces (SI Appendix, Fig. S6 E and F), resulting in a multigap superconducting state with T_c of 138 K ($\mu^* = 0.13$) to 145 K ($\mu^* = 0.10$) at $\varepsilon_{zz} = 0.051$ under the anisotropic compressive stress conditions $\sigma_{xx} = \sigma_{yy} = 350$ GPa and $\sigma_{zz} = 411$ GPa (Fig. 4D).

Discussion

First-principles calculations of stress-strain relations indicate that phase III of solid hydrogen can sustain large anisotropic stresses at megabar pressures, and the accompanying reversible deformations in the elastic region notably alter the crystal symmetry, charge distributions, and bonding behavior. The resulting band shifts, splittings, and enhanced electron-phonon coupling of the phase can dramatically exceed those induced by pure isotropic compression. The effects lead to band gap closure and ensuing superconductivity at significantly reduced compressive stresses compared to hydrostatic conditions. Most notable is shear deformation causing hydrogen to become metallic and superconducting at 250 GPa, which is about 120 GPa (i.e., >30%) lower than that obtained under hydrostatic conditions predicted at the same level of calculation. These results provide specific predictions that could be tested on hydrogen under extreme compression by additional stress conditions that are achievable in the laboratory. Since such stress

anisotropy is in general highly sample and P-T path dependent, the present results may help to explain apparent discrepancies in previously reported experimental results, including variations in rate of bandgap closure and onset of electrical conductivity in solid molecular hydrogen (7, 8, 10–12). Furthermore, stress anisotropy in such compressed materials can be both controlled (e.g., by varying the geometry of thin samples and thermal annealing) and measured with various spectroscopic, diffraction, and imaging techniques (28, 29, 33).

As discussed above, strong deformation of samples can occur under DAC loading, giving rise to potentially significant anisotropic strains (28, 29). Although lateral motion of the anvil can shear the sample due to friction at the sample–anvil interface (30), it should be pointed out that anisotropic strains in the sample in general develop, an effect that is controlled by the elastic/plastic response of the component materials in the biaxial or triaxial stress field produced within the DAC at these conditions. As a result, such complex biaxial or triaxial stress fields can induce significant shear strains in the sample material, as mentioned above. These effects give rise to pressure gradients that can be measured in DAC samples under a variety of conditions (28, 29). These gradients, which are controlled by the sample geometry as well as its elasticity, strength, and plasticity, will project shear stresses into multiple slip planes of the compressed sample (SI Appendix).

We now comment on the possible impact of quantum and thermal effects on the present findings. It has been proposed that the prototypical quantum crystal, low-density solid ^4He , may develop giant nonclassical plasticity (41), but it was also pointed out that the observed phenomenon may be primarily rooted in thermal rather than quantum effects (42), and a later study showed (43) that the stress responses are well described

by classical mechanical theory. Moreover, strength enhancement of solid helium under pressure has been documented (44), and analogous results were observed in hydrogen (45). Experimental studies of other low- Z systems, such as Li, LiH, and LiF, document significant contributions of both thermal (e.g., Debye–Waller) effects and quantum zero-point effects on their lattice dynamics (46, 47). For phase III of hydrogen, anharmonic finite-temperature effects have been shown to reduce the electronic band gaps (24). The quantum nature of the protons and anharmonicity are also predicted to increase the intramolecular distance and enhance superconductivity in molecular hydrogen (48). Thermal effects tend to soften crystals and reduce compressive and shear strengths (49), but probably do not have a large influence on the structural and mechanical behavior at the pressure–temperature regimes of interest here (>200 GPa and <300 K).

In conclusion, this study opens a different avenue and perspective on the metallization and potential high- T_c superconductivity in dense hydrogen under stress conditions possible in high-pressure experiments, most notably static compression studies using diamond anvil cells. The results provide an instructive comparison to many benchmark theoretical studies of molecular hydrogen, i.e., as a classical crystal at the same level of theory under hydrostatic pressures (13, 21–25, 27, 37–39) versus the nonhydrostatic conditions considered in this work. While quantum and thermal effects may modify some predicted quantitative aspects, these effects are not expected to change the trends and alter our principal conclusions about the impact of anisotropic stresses on the electronic properties of hydrogen under pressure. Moreover, the findings have implications for other molecular solids and related systems, which are likely to sustain even higher shear stresses than dense solid hydrogen. These materials include hydride high- T_c superconductors (34, 35, 50–53), whose stability ranges and properties may be significantly altered by anisotropic stresses.

Materials and Methods

We have performed the structural relaxation and stress-strain relation calculations using the Vienna ab initio simulation package (VASP) code,

adopting the projector-augmented wave method and the Perdew–Burke–Ernzerhof generalized-gradient approximation (GGA-PBE) exchange–correlation functional (XC) with 900 eV cutoff energy and $8 \times 9 \times 10$ Monkhorst–Pack k mesh. The stress–strain relations are determined with a strain increment of 0.01, where at each step the applied the shear or compressive strain is fixed to determine the shear stress σ_{xz} or compressive stress σ_{zz} , respectively, while the other five independent components of the strain tensors and all atomic positions are simultaneously relaxed. The second version of the van der Waals density functional (vdW-DF2) XC has been used to calculate the bandgap E_g , electronic band structure, and Fermi surface of molecular hydrogen implemented in VASP code. We have used the QAIM analysis implemented in Atoms in Molecules–Universidad de Carabobo (AIM-UC) software. The lattice dynamics and electron–phonon coupling calculations were performed using the QUANTUM ESPRESSO code, adopting an energy cutoff of 80 Ry and an $8 \times 8 \times 8$ k mesh and $4 \times 4 \times 4$ q mesh (see *SI Appendix, Fig. S7* for the convergence test). The anisotropic superconducting gap and T_c are calculated using the open-source electron–phonon Wannier code. More computational details can be found in *SI Appendix*.

Data Availability. All study data are included in this article and/or *SI Appendix*.

ACKNOWLEDGMENTS. This work was supported by the National Key Research and Development Program of China under Grant 2021YFA1400503; the Natural Science Foundation of China under Grants 52090024, 12074140, and 12034009; the US NSF (DMR-2104881); the US Department of Energy/ National Nuclear Security Administration (DOE/NNSA) (DE-NA0003975); and the Program for the Jilin University (JLU) Science and Technology Innovative Research Team. The reported calculations utilized computing facilities at the High-Performance Computing Center of Jilin University.

Author affiliations: ^aState Key Laboratory of Superhard Materials, College of Physics, Jilin University, Changchun 130012, China; ^bInternational Center for Computational Method and Software, College of Physics, Jilin University, Changchun 130012, China; ^cInternational Center of Future Science, Jilin University, Changchun 130012, China; ^dJilin Provincial International Cooperation Key Laboratory of High-Efficiency Clean Energy Materials, Jilin University, Changchun 130012, China; ^eDepartments of Physics, Chemistry, and Earth and Environmental Sciences, University of Illinois Chicago, Chicago, IL 60607; and ^fDepartment of Physics and Astronomy, University of Nevada, Las Vegas, NV 89154

Author contributions: Q.L., R.J.H., Y.M., and C.C. designed research; X.S. and C.L. performed research; X.S., C.L., Q.L., Y.M., and C.C. analyzed data; and X.S., C.L., Q.L., R.J.H., Y.M., and C.C. wrote the paper.

1. E. Wigner, H. B. Huntington, On the possibility of a metallic modification of hydrogen. *J. Chem. Phys.* **3**, 764–770 (1935).
2. H. K. Mao, R. J. Hemley, Ultrahigh-pressure transitions in solid hydrogen. *Rev. Mod. Phys.* **66**, 671–692 (1994).
3. J. M. McMahon, M. A. Morales, C. Pierleoni, D. M. Ceperley, The properties of hydrogen and helium under extreme conditions. *Rev. Mod. Phys.* **84**, 1607–1653 (2012).
4. N. W. Ashcroft, Metallic hydrogen: A high-temperature superconductor? *Phys. Rev. Lett.* **21**, 1748 (1968).
5. L. J. Zhang, Y. C. Wang, J. Lv, Y. M. Ma, Materials discovery at high pressures. *Nat. Rev. Mater.* **2**, 17005 (2017).
6. R. J. Hemley, H. K. Mao, Phase transition in solid molecular hydrogen at ultrahigh pressures. *Phys. Rev. Lett.* **61**, 857–860 (1988).
7. H. K. Mao, R. J. Hemley, Optical studies of hydrogen above 200 gigapascals: Evidence for metallization by band overlap. *Science* **244**, 1462–1465 (1989).
8. C. Narayana, H. Luo, J. Orloff, A. L. Ruoff, Solid hydrogen at 342 GPa: No evidence for an alkali metal. *Nature* **393**, 46–49 (1998).
9. A. F. Goncharov, E. Gregoryanz, R. J. Hemley, H. Mao, Spectroscopic studies of the vibrational and electronic properties of solid hydrogen to 285 GPa. *Proc. Natl. Acad. Sci. U.S.A.* **98**, 14234–14237 (2001).
10. P. Loubeyre, F. Occelli, R. LeToullec, Optical studies of solid hydrogen to 320 GPa and evidence for black hydrogen. *Nature* **416**, 613–617 (2002).
11. M. I. Erements, I. A. Troyan, Conductive dense hydrogen. *Nat. Mater.* **10**, 927–931 (2011).
12. C. S. Zha, Z. Liu, R. J. Hemley, Synchrotron infrared measurements of dense hydrogen to 360 GPa. *Phys. Rev. Lett.* **108**, 146402 (2012).
13. A. F. Goncharov *et al.*, Bonding, structures, and band gap closure of hydrogen at high pressures. *Phys. Rev. B Condens. Matter Mater. Phys.* **87**, 024101 (2013).
14. R. P. Dias, I. F. Silvera, Observation of the Wigner–Huntington transition to metallic hydrogen. *Science* **355**, 715–718 (2017).
15. M. I. Erements, A. P. Drozdov, P. P. Kong, H. Wang, Semimetallic molecular hydrogen at pressure above 350 GPa. *Nat. Phys.* **15**, 1246–1249 (2019).
16. P. Loubeyre, F. Occelli, P. Dumas, Synchrotron infrared spectroscopic evidence of the probable transition to metal hydrogen. *Nature* **577**, 631–635 (2020).
17. C. J. Pickard, R. J. Needs, Structure of phase III of solid hydrogen. *Nat. Phys.* **3**, 473–476 (2007).
18. C. J. Pickard, M. Martinez-Canales, Density functional theory study of phase IV of solid hydrogen. *Phys. Rev. B Condens. Matter Mater. Phys.* **85**, 214114 (2012).
19. J. McMinis, R. C. Clay III, D. Lee, M. A. Morales, Molecular to atomic phase transition in hydrogen under high pressure. *Phys. Rev. Lett.* **114**, 105305 (2015).
20. P. Dalladay-Simpson, R. T. Howie, E. Gregoryanz, Evidence for a new phase of dense hydrogen above 325 gigapascals. *Nature* **529**, 63–67 (2016).
21. B. Monserrat *et al.*, Structure and metallicity of phase V of hydrogen. *Phys. Rev. Lett.* **120**, 255701 (2018).
22. M. A. Morales, J. F. McMahon, C. Pierleoni, D. M. Ceperley, Towards a predictive first-principles description of solid molecular hydrogen with density functional theory. *Phys. Rev. B Condens. Matter Mater. Phys.* **87**, 184107 (2013).
23. I. I. Naumov, R. E. Cohen, R. J. Hemley, Graphene physics and insulator-metal transition in compressed hydrogen. *Phys. Rev. B Condens. Matter Mater. Phys.* **88**, 045125 (2013).
24. R. Singh, S. Azadi, T. D. Kuhne, Anharmonicity and finite-temperature effects on the structure, stability, and vibrational spectrum of phase III of solid molecular hydrogen. *Phys. Rev. B Condens. Matter Mater. Phys.* **90**, 014110 (2014).
25. S. Azadi, N. D. Drummond, W. M. C. Foulkes, Nature of the metallization transition in solid hydrogen. *Phys. Rev. B Condens. Matter Mater. Phys.* **95**, 035142 (2017).
26. W. L. Yim, H. L. Shi, Y. F. Liang, R. J. Hemley, J. S. Tse, “Band gaps and effective oscillator models for solid hydrogen and H₂O ice at high pressure” in *Correlations in Condensed Matter under Extreme Conditions*, G. G. N. Angilella, A. La Magna, Eds. (World Scientific, 2017), pp. 107–126.
27. L. Monacelli, I. Errea, M. Calandra, F. Mauri, Black metal hydrogen above 360 GPa driven by proton quantum fluctuations. *Nat. Phys.* **17**, 63–67 (2021).
28. R. J. Hemley *et al.*, X-ray imaging of stress and strain of diamond, iron, and tungsten at megabar pressures. *Science* **276**, 1242–1245 (1997).
29. B. Li *et al.*, Diamond anvil cell behavior up to 4 Mbar. *Proc. Natl. Acad. Sci. U.S.A.* **115**, 1713–1717 (2018).
30. V. I. Levitas, M. Kamrani, B. Feng, Tensorial stress-strain fields and large elastoplasticity as well as friction in diamond anvil cell up to 400 GPa. *npj Comput. Mater.* **5**, 94 (2019).
31. C. Liu, X. Song, Q. Li, Y. Ma, C. Chen, Smooth flow in diamond: Atomistic ductility and electronic conductivity. *Phys. Rev. Lett.* **123**, 195504 (2019).
32. Z. Shi *et al.*, Metallization of diamond. *Proc. Natl. Acad. Sci. U.S.A.* **117**, 24634–24639 (2020).

33. H. K. Mao, J. Badro, J. Shu, R. J. Hemley, A. K. Singh, Strength, anisotropy, and preferred orientation of solid argon at high pressures. *J. Phys. Condens. Matter* **18**, S963-S968 (2006).
34. M. Somayazulu *et al.*, Evidence for superconductivity above 260 K in lanthanum superhydride at megabar pressures. *Phys. Rev. Lett.* **122**, 027001 (2019).
35. A. P. Drozdov *et al.*, Superconductivity at 250 K in lanthanum hydride under high pressures. *Nature* **569**, 528-531 (2019).
36. J. S. Tse, D. D. Klug, Y. S. Yao, Y. L. Page, J. R. Rodgers, Structure and spectroscopic properties of dense solid hydrogen at 160 GPa. *Solid State Commun.* **145**, 5-10 (2008).
37. L. J. Zhang *et al.*, *Ab initio* prediction of superconductivity in molecular metallic hydrogen under high pressure. *Solid State Commun.* **141**, 610-614 (2007).
38. P. Cudazzo *et al.*, *Ab initio* description of high-temperature superconductivity in dense molecular hydrogen. *Phys. Rev. Lett.* **100**, 257001 (2008).
39. P. Cudazzo *et al.*, Electron-phonon interaction and superconductivity in metallic molecular hydrogen. II. Superconductivity under pressure. *Phys. Rev. B Condens. Matter Mater. Phys.* **81**, 134506 (2010).
40. P. Cudazzo *et al.*, Electron-phonon interaction and superconductivity in metallic molecular hydrogen. I. Electronic and dynamical properties under pressure. *Phys. Rev. B Condens. Matter Mater. Phys.* **81**, 134505 (2010).
41. A. Haziot, X. Rojas, A. D. Fefferman, J. R. Beamish, S. Balibar, Giant plasticity of a quantum crystal. *Phys. Rev. Lett.* **110**, 035301 (2013).
42. C. Zhou *et al.*, Comment on "Giant plasticity of a quantum crystal". *Phys. Rev. Lett.* **111**, 119601 (2013).
43. E. J. L. Borda, W. Cai, M. de Koning, Ideal shear strength of a quantum crystal. *Phys. Rev. Lett.* **112**, 155303 (2014).
44. C. S. Zha, H. K. Mao, R. J. Hemley, Elasticity of dense helium. *Phys. Rev. B Condens. Matter Mater. Phys.* **70**, 174107 (2004).
45. C. S. Zha, T. S. Duffy, H. K. Mao, R. J. Hemley, Elasticity of hydrogen to 24 GPa from single-crystal Brillouin scattering and synchrotron x-ray diffraction. *Phys. Rev. B Condens. Matter Mater. Phys.* **48**, 9246-9255 (1993).
46. C. Sternemann *et al.*, Influence of lattice dynamics on electron momentum density of lithium. *J. Phys. Chem. Solids* **61**, 379 (2000).
47. G. Dolling, H. G. Smith, R. M. Nicklow, P. R. Vijayaraghavan, M. K. Wilkinson, Lattice dynamics of lithium fluoride. *Phys. Rev.* **168**, 970 (1968).
48. M. Borinaga *et al.*, Anharmonic enhancement of superconductivity in metallic molecular Cmca - 4 hydrogen at high pressure: A first-principles study. *J. Phys. Condens. Matter* **28**, 494001 (2016).
49. L. Wen, H. Wu, H. Sun, C. F. Chen, Profound softening and shear-induced melting of diamond under extreme conditions: An ab-initio molecular dynamics study. *Carbon* **155**, 361-368 (2019).
50. H. Wang, J. S. Tse, K. Tanaka, T. Iitaka, Y. Ma, Superconductive sodalite-like clathrate calcium hydride at high pressures. *Proc. Natl. Acad. Sci. U.S.A.* **109**, 6463-6466 (2012).
51. F. Peng *et al.*, Hydrogen clathrate structures in rare earth hydrides at high pressures: Possible route to room-temperature superconductivity. *Phys. Rev. Lett.* **119**, 107001 (2017).
52. H. Liu, I. I. Naumov, R. Hoffmann, N. W. Ashcroft, R. J. Hemley, Potential high- T_c superconducting lanthanum and yttrium hydrides at high pressure. *Proc. Natl. Acad. Sci. U.S.A.* **114**, 6990-6995 (2017).
53. E. Snider *et al.*, Room-temperature superconductivity in a carbonaceous sulfur hydride. *Nature* **586**, 373-377 (2020).

Supplementary Information for

Stress-Induced High- T_c Superconductivity in Solid Molecular Hydrogen

Xianqi Song, Chang Liu, Quan Li, Russell J. Hemley, Yanming Ma, and Changfeng Chen

Quan Li

E-mail: liquan777@jlu.edu.cn

Russell J. Hemley

E-mail: rhemley@uic.edu

Yanming Ma

E-mail: mym@jlu.edu.cn

Changfeng Chen

E-mail: changfeng.chen@unlv.edu

This PDF file includes:

Supplementary text

Figs. S1 to S7

Table S1

SI References

Supporting Information Text

Here we provide the expanded discussions about non-hydrostatic stress states in diamond anvil cells (DACs), a systematic description of computational methods, and additional details supporting several results in the main text, including stress response under various shear or compressive strains, evolution of electronic bandgap under hydrostatic pressure and different loading conditions, QTAIM analysis, bond length, Fermi surfaces, the convergence test, and crystal structures of molecular hydrogen.

Anisotropic stress-strain states in DAC samples. Complex stress-strain states typically develop in megabar (>100 GPa) studies of solids in DACs, particularly at low or modest temperatures (e.g., <300 K in hydrogen). Non-hydrostatic states are controlled by sample material properties (including grain-grain interactions) and strong deformations of the diamond tip, sample and gasket. Pressure distribution models suggest maximum shear stresses in DAC could reach $0.29P_s$ to $0.38P_s$ where P_s is the peak axial stress/pressure inside DAC (1–3). Many studies over the decades show that there can be a large distribution of pressure/stress states from the center to edge of the DAC sample, effects that depend on sample strength, elasticity, and shape (e.g., thickness). These phenomena have been explored in recent theoretical investigations (4, 5), and a recent experimental study of DAC samples that builds on an early work to 300 GPa (6) further explores the pressure loading, distribution, gasket-thickness variation, and diamond anvil deformation up to 400 GP (7). For solid hydrogen at megabar pressures, we expect that these factors give rise to projected shear stresses in many shear-slip planes in the sample regardless of the orientation of the sample crystals. We also note that large shear stresses can be introduced in specific DAC experiments using rotational diamond anvil cells. These experiments have led to the discovery of novel phenomena such as shear-driven formation of diamond (8) and significant changes in phase transformation paths of other materials (9).

Methods. We performed the structural relaxation and stress-strain relation calculations using the Vienna Ab-initio Simulation Package (VASP) code (10), adopting the projector-augmented wave (PAW) method with the hydrogen $1s^1$ electron (cutoff radius 1.1 au) treated as the valence electron and the generalized gradient approximation (GGA) exchange-correlation functional (XC) within the framework of Perdew-Burke-Ernzerh (PBE) (11, 12). We selected 900 eV cutoff energy and $8 \times 9 \times 10$ Monkhorst-Pack k -mesh (13) to ensure all the enthalpy calculations are converged to better than 1 meV/atom. The stress-strain relations were determined using an established method (14–19) with a strain increment of 0.01, where at each step the applied the shear or compressive strain is fixed to determine the shear stress σ_{xz} or compressive stress σ_{zz} , respectively, while the other five independent components of the strain tensors and all atomic positions are simultaneously relaxed with residual forces and stresses less than 0.005 eV/Å and 0.1 GPa, respectively. It is known that GGA-PBE XC usually underestimates the electronic bandgap E_g , we thus estimated E_g values using GGA-PBE XC, vdW-DF2 XC (20), and the GW method (21) (see Fig. S3). The single-shot GW (G_0W_0) calculations, starting from GGA Kohn-Sham eigenvalues and wave functions, were performed in the VASP code interfaced with the Wannier90 and core-valence interactions are treated on the DFT level. It is seen that vdW-DF2 non-local XC (different from the vdW correction based on semi-empirical force field models) gives a good description of E_g and thus has been selected to calculate the electronic band structure and Fermi surface of molecular hydrogen (22). It is noted that while not accounting for the long-range Fock interactions like hybrid functionals or GW, the vdW-DF2 functional has been extensively studied and tested for describing the bandgap of dense molecular hydrogen. The results show that vdW-DF2 consistently generates bandgap values close to those obtained using the HSE functional at high pressure (23, 24). Moreover, we tested vdW-DF2 versus GW in describing the bandgap of solid molecular hydrogen at selected pressures and found that vdW-DF2 produces results in good agreement with those from GW calculations (Fig. S3). Considering the computational cost of HSE or GW, it is advantageous to use vdW-DF2 that offers an efficient tool with reasonable accuracy based on its verified consistent performance, albeit established at an empirical level. The 3D Fermi surfaces are visualized by XCrySDen software (25). We used the quantum theory of atoms in molecules (QTAIM) analysis implemented in AIM-UC software (26, 27). The lattice dynamics and electron-phonon coupling (EPC) calculations were performed using QUANTUM ESPRESSO (QE) code (28) in the framework of density-functional perturbation theory (DFPT) (29), adopting an energy cutoff of 80 Ry and an $8 \times 8 \times 8$ k mesh in the PAW-PBE framework, which offers an adequate description of the metallic states and phonon-mediated superconductivity (30–33). The lattice dynamics calculations used a $4 \times 4 \times 4$ q mesh. Under strain, deformed hydrogen crystal exhibits progressively reduced symmetry that leads to a substantially increased number of irreducible q points in the electron-phonon calculations, for example, the number of irreducible q -points within the $3 \times 3 \times 3$, $4 \times 4 \times 4$, and $5 \times 5 \times 5$ q -mesh is 14, 36, and 63 at shear strain $\varepsilon_{zx} = 0.138$ in (001)[010] direction at 250 GPa, respectively. We show in Fig. S7 the calculated superconducting critical temperatures (T_c) versus Gaussian spreading with various choices of k and q mesh. We adopted the common practice of testing convergence and calculating T_c using a small Gaussian smearing width. Specifically, under a smearing width of 0.04 Ry, the $8 \times 8 \times 8$ k -mesh and $4 \times 4 \times 4$ q -mesh used in this work produces T_c values that are converged to within about 5 K (see results shown in Fig. S7). The anisotropic superconducting gap and consequent T_c were calculated using the open-source Electron-phonon Wannier code (34).

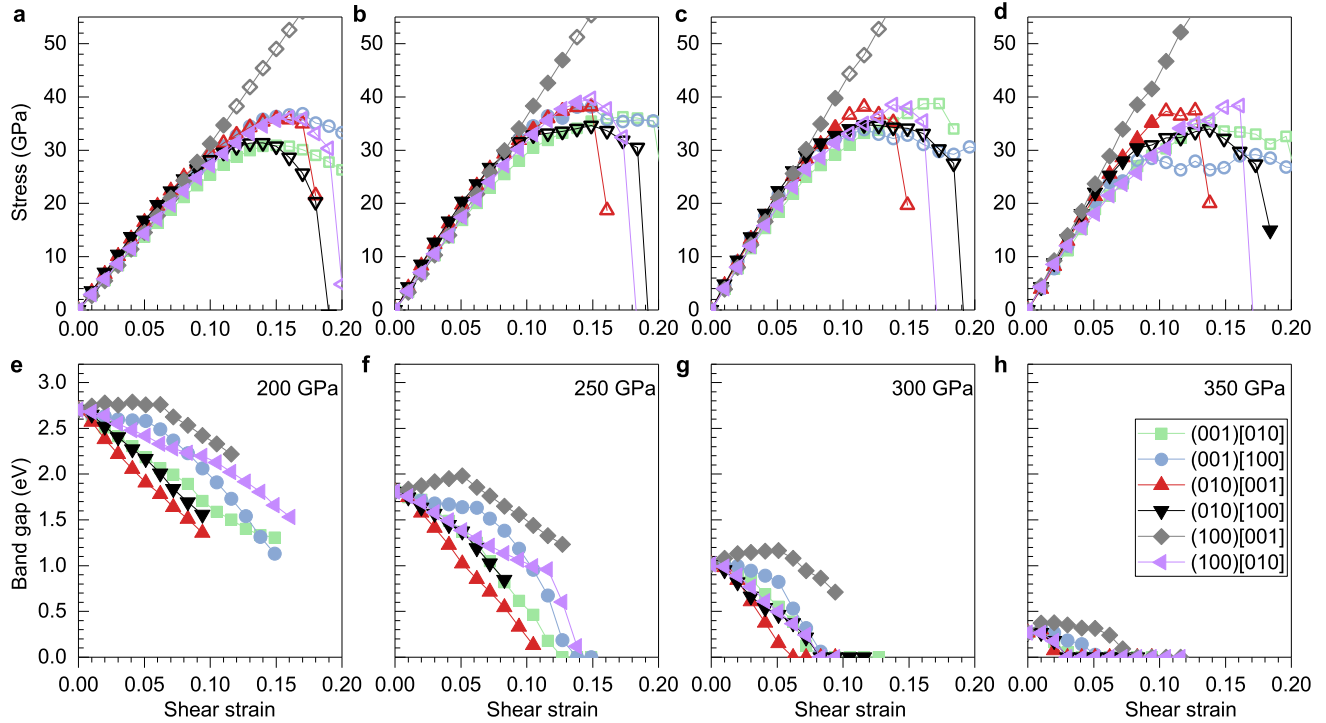


Fig. S1. The calculated shear-stress response and electronic bandgap (E_g) evolution of the $C2/c$ phase of solid molecular hydrogen. (a-d) The shear stress-strain ($\sigma_{zx}-\epsilon_{zx}$) relations, where the hollow symbols indicate dynamic instability of the deformed structure, at 200, 250, 300, and 350 GPa, respectively. (e-h) The E_g of deformed solid molecular hydrogen along the shear-strain paths at 200, 250, 300, and 350 GPa, respectively, up to the dynamic stability limit.

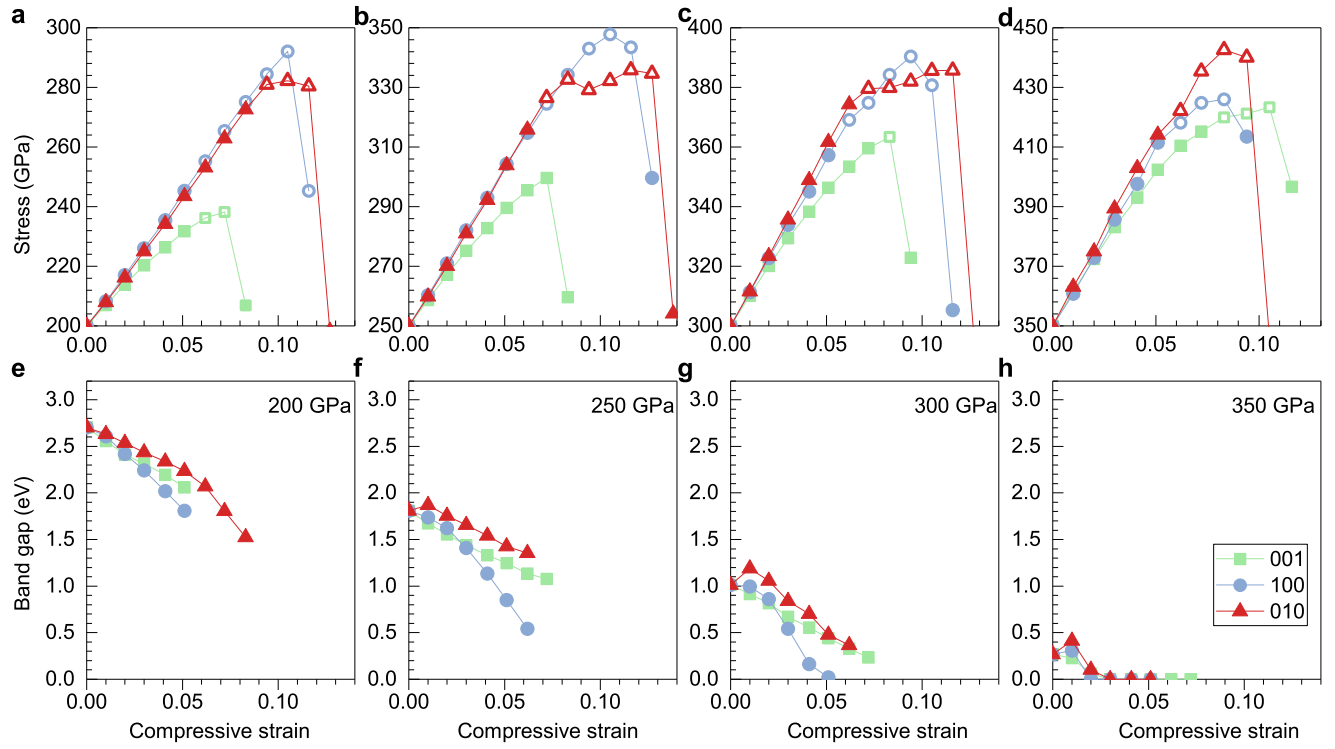


Fig. S2. The calculated compressive-stress response and electronic bandgap (E_g) evolution of the $C2/c$ phase of solid molecular hydrogen. (a-d) The compressive stress-strain ($\sigma_{zz} - \epsilon_{zz}$) relations, where the hollow symbols indicate dynamic instability of the deformed structure, at 200, 250, 300, and 350 GPa, respectively. (e-h) The E_g of deformed solid molecular hydrogen along the compressive-strain paths at 200, 250, 300, and 350 GPa, respectively, up to the dynamic stability limit.

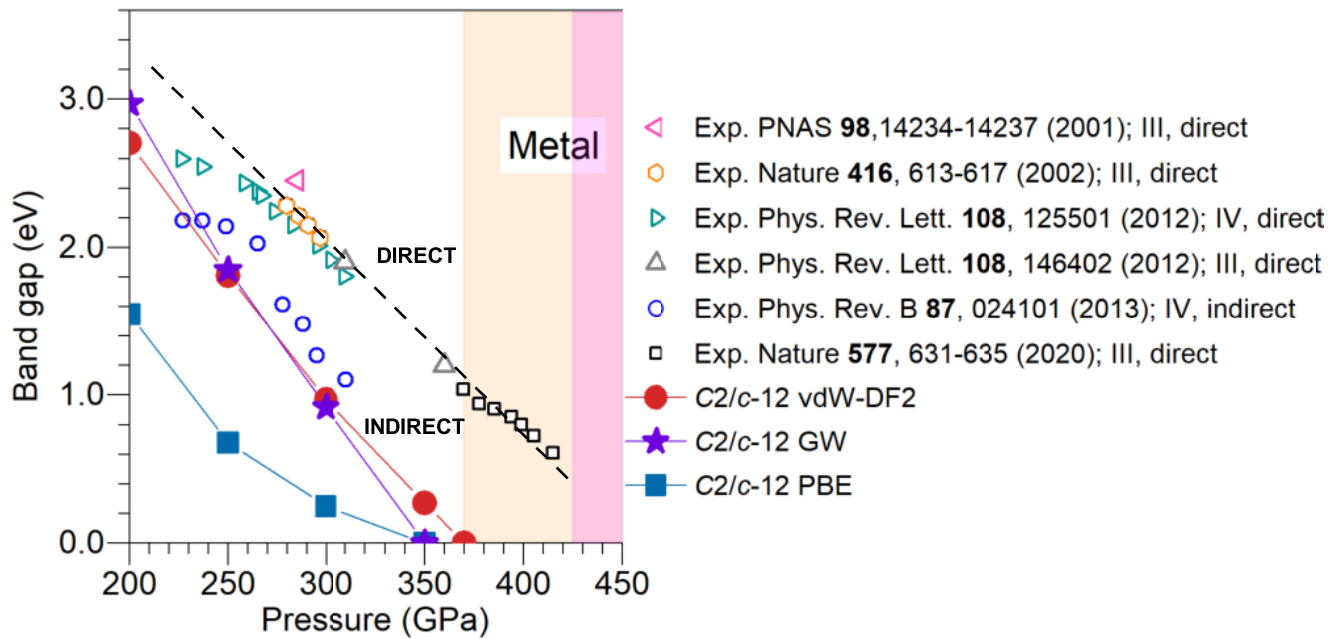


Fig. S3. The electronic band gap versus hydrostatic pressures: comparison between experimental data (all open symbols) for both phases III and IV and calculated results from previously reported and present work (solid symbols). The orange and pink shaded regions indicate the estimated transition pressures to metallic hydrogen proposed by Eremets *et al.* (35) and Loubeyre *et al.* (36), respectively; see also Zha *et al.* (37). The E_g values are calculated for the indirect gaps using the GGA-PBE XC, vdW-DF2 XC, and GW methods, as shown by the indigo square, red circular, and purple star symbols, respectively. Similar results were obtained by Lebègue *et al.* (38) and by Yim *et al.* (39) and correspond to the model structure for phase III. Considering the accuracy and efficiency, we have selected the vdW-DF2 XC for the calculations of electronic properties, such as electronic band structure, Fermi surface, and QTAIM analysis presented in this work.

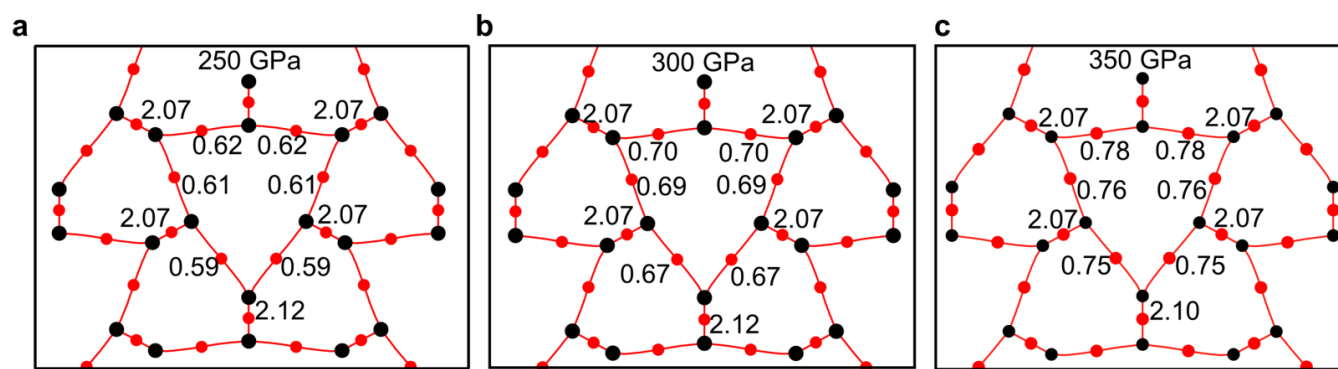


Fig. S4. The crystal structure and charge density in the atomic unit based on a QTAIM analysis of the $C2/c$ H_2 phase of solid molecular hydrogen at hydrostatic pressure of (a) 250 GPa, (b) 300 GPa, and (c) 350 GPa. The large black spheres represent the hydrogen atoms and the small red spheres are bond critical points (BCPs). The charge density values at the BCPs above 2.00 a.u. describe the intramolecular covalent bonds of the hydrogen molecules and the charge density values of 0.50~0.80 a.u. characterize the intermolecular Van der Waals interaction between the hydrogen molecules.

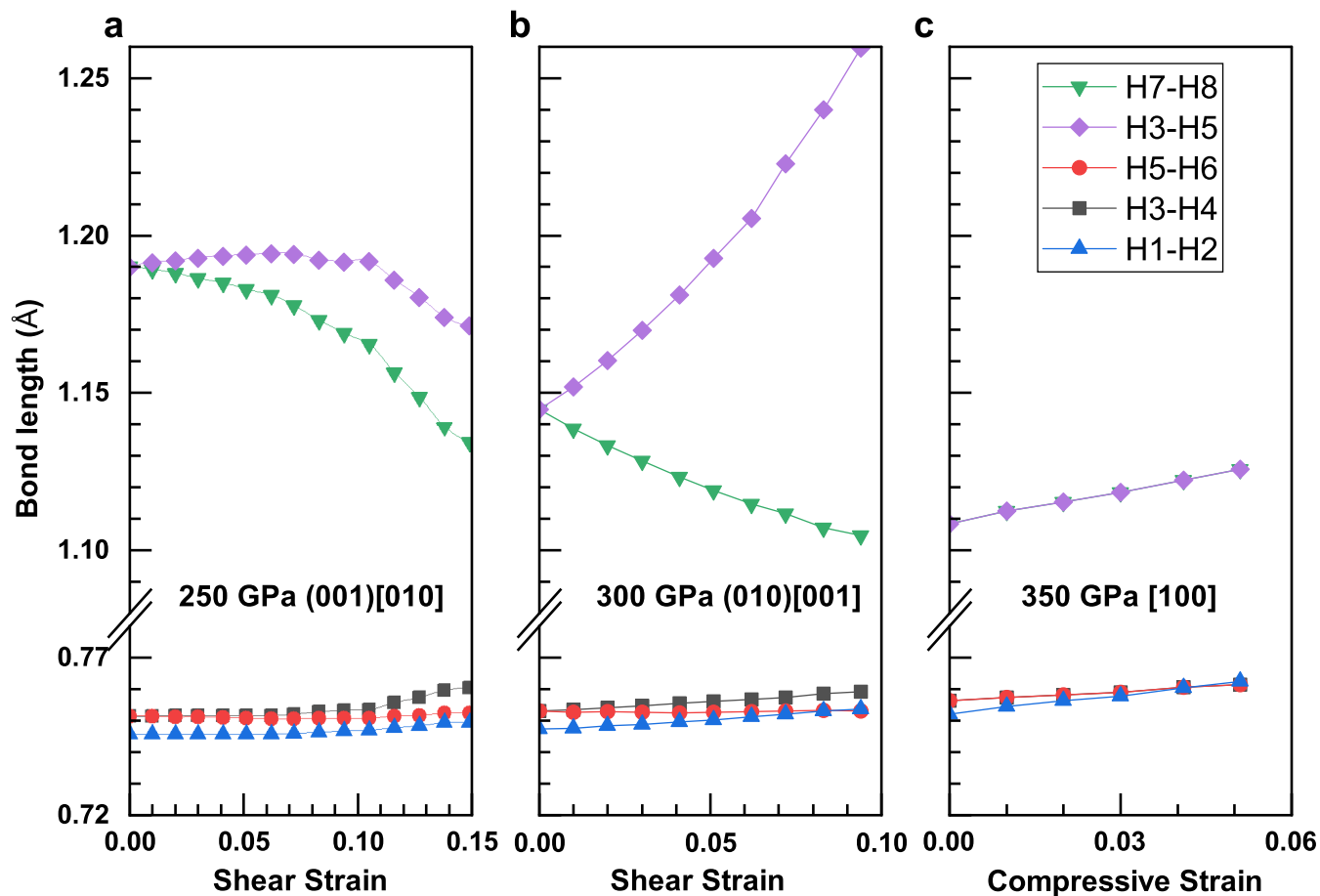


Fig. S5. The evolution of hydrogen atomic distance under different loading paths: (a) the shear strain in the (001)[010] direction at 250 GPa; (b) the shear strain in the (010)[001] direction at 300 GPa; (c) the compressive strain in the [100] direction at 350 GPa.

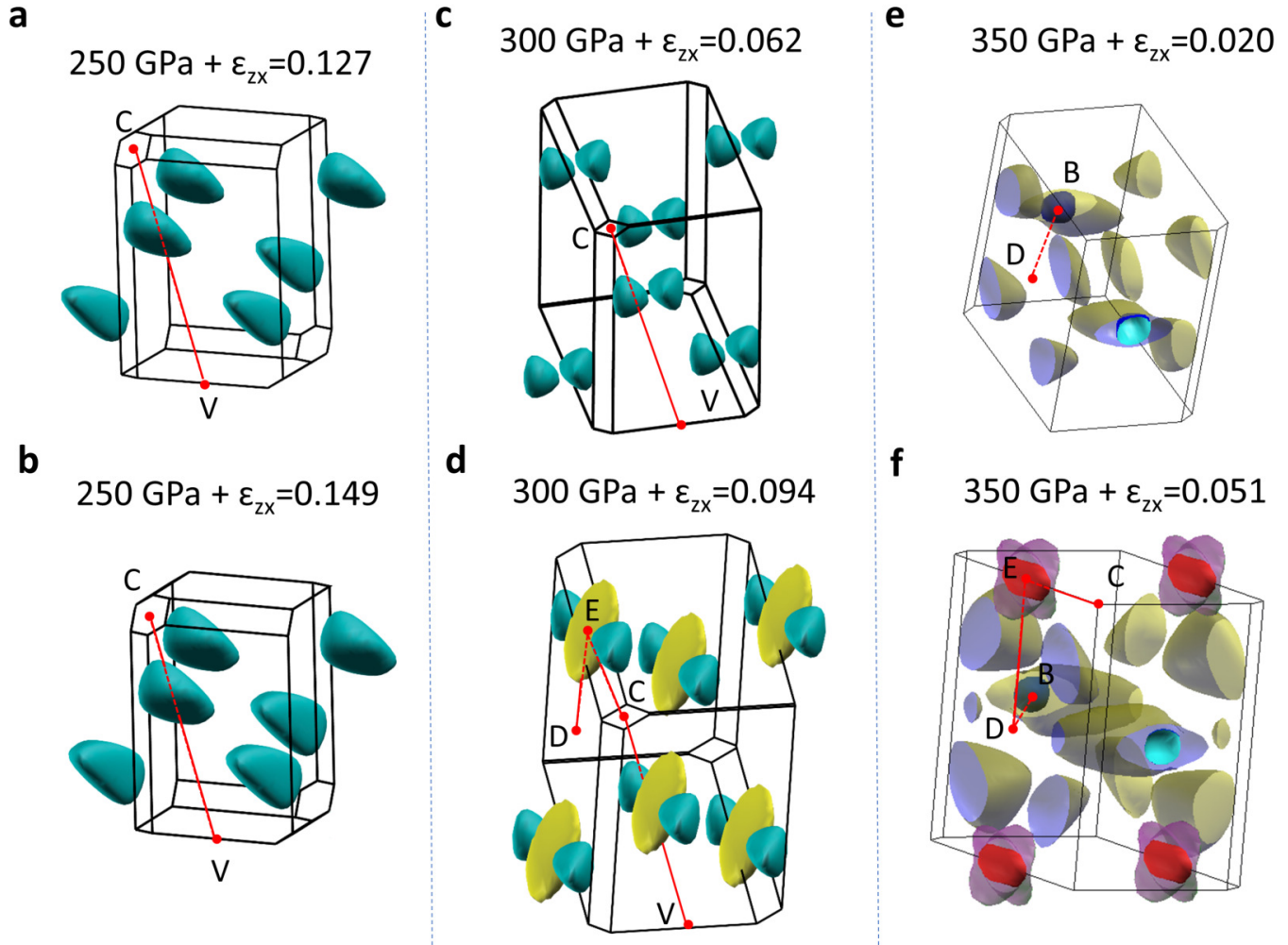


Fig. S6. The calculated three-dimensional Fermi surfaces of the $C2/c$ H_2 phase of solid molecular hydrogen. (a,b) The hole-type Fermi-surface pockets of shear deformed solid molecular hydrogen at 250 GPa, which grows with increasing strains. (c) The hole-type Fermi-surface pocket of shear deformed $C2/c$ solid molecular hydrogen at 300 GPa under the shear strain $\epsilon_{zx}=0.062$. (d) The hole- and electron-type Fermi-surface pockets of shear deformed $C2/c$ solid molecular hydrogen at 300 GPa under the shear strain $\epsilon_{zx}=0.094$. (e) The double hole-type Fermi-surface pockets of compressive deformed $C2/c$ solid molecular hydrogen at 350 GPa under compressive strain $\epsilon_{zz}=0.020$. (f) The double hole-type and double electron-type Fermi-surface pockets of compressive deformed $C2/c$ solid molecular hydrogen at 350 GPa under compressive strain $\epsilon_{zz}=0.051$. The black solid cells outline the first Brillouin zone and the red lines are the k -point paths.

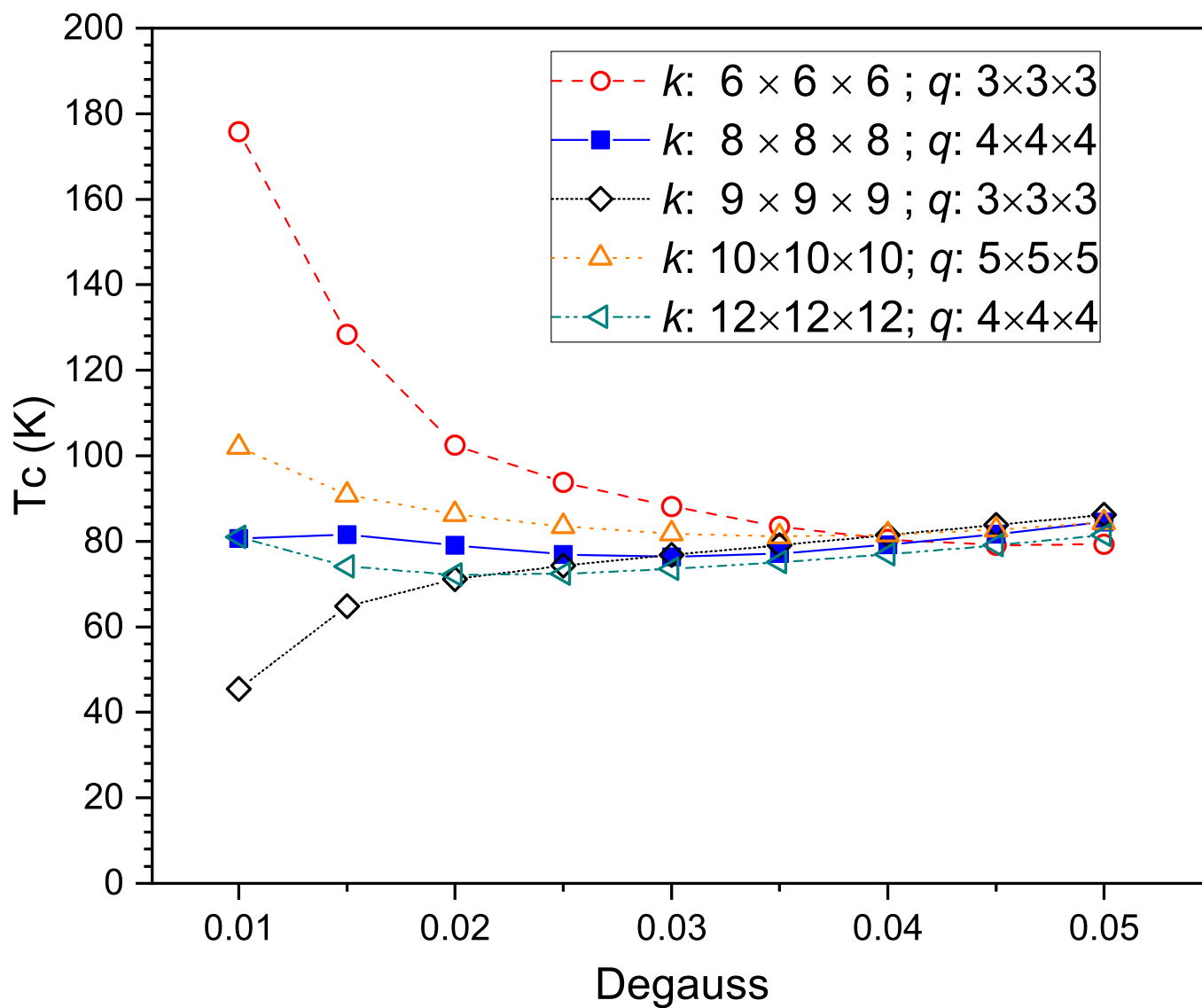


Fig. S7. The convergence test to T_c of $C2/c$ molecular hydrogen at shear strain $\varepsilon_{zx} = 0.138$ in (001)[010] direction at 250 GPa versus Gaussian spreading with various choices of k and q mesh.

Table S1. The crystal structure information of representative deformed molecular hydrogen

250 GPa (001)[010] $\varepsilon_{zx}=0.149$				300 GPa (010)[001] $\varepsilon_{zx}=0.094$				350 GPa [100] $\varepsilon_{zz}=0.051$			
Parameters	x	y	z	Parameters	x	y	z	Parameters	x	y	z
$a=5.029 \text{ \AA}$	0.224	0.073	0.236	$a=4.918 \text{ \AA}$	0.219	0.079	0.240	$a=4.803 \text{ \AA}$	0.225	0.069	0.250
$b=2.876 \text{ \AA}$	0.776	0.927	0.764	$b=2.843 \text{ \AA}$	0.781	0.921	0.760	$b=2.765 \text{ \AA}$	0.775	0.931	0.750
$c=4.253 \text{ \AA}$	0.764	0.072	0.249	$c=4.130 \text{ \AA}$	0.765	0.070	0.248	$c=4.134 \text{ \AA}$	0.775	0.069	0.250
$\alpha=85.165^\circ$	0.236	0.928	0.751	$\alpha=84.896^\circ$	0.235	0.930	0.752	$\alpha=90.000^\circ$	0.225	0.931	0.750
$\beta=141.598^\circ$	0.724	0.573	0.236	$\beta=142.510^\circ$	0.719	0.579	0.240	$\beta=144.419^\circ$	0.725	0.569	0.250
$\gamma=89.923^\circ$	0.276	0.427	0.764	$\gamma=93.848^\circ$	0.281	0.421	0.760	$\gamma=90.000^\circ$	0.275	0.431	0.750
	0.264	0.572	0.249		0.265	0.570	0.248		0.275	0.569	0.250
	0.736	0.428	0.751		0.735	0.430	0.752		0.725	0.431	0.750
	0.347	0.206	0.227		0.354	0.179	0.225		0.348	0.193	0.225
	0.653	0.794	0.773		0.646	0.821	0.775		0.652	0.807	0.775
	0.665	0.211	0.289		0.662	0.208	0.281		0.652	0.193	0.275
	0.335	0.789	0.711		0.338	0.792	0.719		0.348	0.807	0.725
	0.847	0.706	0.227		0.854	0.679	0.225		0.848	0.693	0.225
	0.153	0.294	0.773		0.146	0.321	0.775		0.152	0.307	0.775
	0.165	0.711	0.289		0.162	0.708	0.281		0.152	0.693	0.275
	0.835	0.289	0.711		0.838	0.292	0.719		0.848	0.307	0.725
	0.490	0.129	0.739		0.491	0.134	0.740		0.500	0.126	0.750
	0.510	0.871	0.261		0.509	0.866	0.260		0.500	0.874	0.250
	0.990	0.629	0.739		0.991	0.634	0.740		0.000	0.626	0.750
	0.010	0.371	0.261		0.009	0.366	0.260		0.000	0.374	0.250
	0.508	0.386	0.754		0.511	0.399	0.747		0.500	0.402	0.750
	0.492	0.614	0.246		0.489	0.601	0.253		0.500	0.598	0.250
	0.008	0.886	0.754		0.011	0.899	0.747		0.000	0.902	0.750
	0.992	0.114	0.246		0.989	0.101	0.253		0.000	0.098	0.250

References

1. A. L. Ruoff, H. Luo, Pressure strengthening: A possible route to obtaining 9 Mbar and metallic diamonds. *J. Appl. Phys.* **70**, 2066 (1991).
2. M. P. Surh, S. G. Louie, M. L. Cohen, Band gaps of diamond under anisotropic stress. *Phys. Rev. B* **45**, 8239 (1992).
3. S. Merkel, R. J. Hemley, H. Mao, Finite-element modeling of diamond deformation at multimegabar pressures. *Appl. Phys. Lett.* **74**, 656 (1999).
4. B. Feng, V. I. Levitas, W. Li, FEM modeling of plastic flow and strain-induced phase transformation in BN under high pressure and large shear in a rotational diamond anvil cell. *Int. J. Plasticity* **113**, 236 (2019).
5. V. I. Levitas, M. Kamrani, B. Feng, Tensorial stress-strain fields and large elastoplasticity as well as friction in diamond anvil cell up to 400 GPa. *npj Comput. Mater.* **5**, 94 (2019).
6. R. J. Hemley *et al.*, X-ray imaging of stress and strain of diamond, iron, and tungsten at megabar pressures. *Science* **276**, 1242-1245 (1997).
7. B. Li *et al.*, Diamond anvil cell behavior up to 4 Mbar. *Proc. Natl. Acad. Sci. U.S.A.* **115**, 1713 (2018).
8. J. Dong *et al.*, Decompression-Induced Diamond Formation from Graphite Sheared under Pressure. *Phys. Rev. Lett.* **124**, 065701 (2020).
9. Y. Gao *et al.*, Shear driven formation of nano-diamonds at sub-gigapascals and 300 K. *Carbon* **146**, 364 (2019).
10. G. Kresse, L. Furthmüller, Efficient iterative schemes for ab initio total-energy calculations using a plane-wave basis set. *Phys. Rev. B* **54**, 11169 (1996).
11. G. Kresse, J. Joubert, From ultrasoft pseudopotentials to the projector augmented-wave method. *Phys. Rev. B* **59**, 1758 (1999).
12. J. P. Perdew, K. Burke, M. Ernzerhof, Generalized Gradient Approximation Made Simple. *Phys. Rev. Lett.* **77**, 3865 (1996).
13. H. J. Monkhorst, J. D. Pack, Special points for Brillouin-zone integrations. *Phys. Rev. B* **13**, 5188 (1976).
14. Y. Zhang, H. Sun, C. F. Chen, Superhard Cubic Compared to Diamond. *Phys. Rev. Lett.* **93**, 195504 (2004).
15. Z. C. Pan, H. Sun, C. F. Chen, Colossal Shear-Strength Enhancement of Low-Density Cubic by Nanoindentation. *Phys. Rev. Lett.* **98**, 135505 (2007).
16. Z. C. Pan, H. Sun, C. F. Chen, Indenter-angle-sensitive fracture modes and stress response at incipient plasticity. *Phys. Rev. B* **79**, 104102 (2009).
17. Z. C. Pan, H. Sun, C. F. Chen, Harder than diamond: superior indentation strength of wurtzite BN and lonsdaleite. *Phys. Rev. Lett.* **102**, 055503 (2009).
18. C. Liu, X. Q. Song, Q. Li, Y. M. Ma, C. F. Chen, Superconductivity in compression-shear deformed diamond. *Phys. Rev. Lett.* **124**, 147001 (2020).
19. C. Liu, X. Q. Song, Q. Li, Y. M. Ma, C. F. Chen, Superconductivity in Shear Strained Semiconductors. *Chin. Phys. Lett.* **38**, 086301 (2021).
20. K. Lee, E. D. Murray, L. Kong, B. I. Lundqvist, D. C. Langreth, Higher-accuracy van der Waals density functional, *Phys. Rev. B* **82**, 081101 (2010).
21. M. Shishkin, G. Kresse, Implementation and performance of the frequency-dependent GW method within the PAW framework. *Phys. Rev. B* **74**, 035101 (2006).
22. S. Azadi, G. J. Ackland, The role of van der Waals and exchange interactions in high-pressure solid hydrogen. *Phys. Chem. Chem. Phys.* **19**, 21829-21839 (2017).
23. V. Gorelov, D. M. Ceperley, M. Holzmann, C. Pierleoni, Electronic energy gap closure and metal-insulator transition in dense liquid hydrogen. *Phys. Rev. B* **102**, 195133 (2020).
24. V. Gorelov, M. Holzmann, D. M. Ceperley, C. Pierleoni, Energy Gap Closure of Crystalline Molecular Hydrogen with Pressure. *Phys. Rev. Lett.* **124**, 116401 (2020).
25. A. Kokalj, XCrySDen—new program for displaying crystalline structures and electron densities. *J. Mol. Graphics Mod.* **17**, 176-179 (1999).
26. R. F. W. Bader, *Molecules, Atoms in Molecules - A Quantum Theory* Clarendon. Oxford University Press, Oxford (1990).
27. D. Vega, D. Almeida, AIM-UC: An application for QTAIM analysis. *J. Comput. Methods Sci. Eng.* **14**, 131-136 (2014).
28. P. Giannozzi *et al.*, QUANTUM ESPRESSO: a modular and open-source software project for quantum simulations of materials. *J. Phys. Condens. Matter.* **21**, 395502 (2009).
29. S. Baroni, S. de Gironcoli, A. D. Corso, P. Giannozzi, Phonons and related crystal properties from density-functional perturbation theory. *Rev. Mod. Phys.* **73**, 515-562 (2001).
30. Y. W. Li, J. Hao, H. Y. Liu, Y. L. Li, Y. M. Ma, The metallization and superconductivity of dense hydrogen sulfide. *J. Chem. Phys.* **140**, 174712 (2014).
31. D. F. Duan *et al.*, Pressure-induced metallization of dense (H₂S)₂H₂ with high-*T_c* superconductivity. *Sci. Rep.* **4**, 6968 (2015).
32. Y. Sun, J. Lv, Y. Xie, H. Y. Liu, Y. M. Ma, Route to a Superconducting Phase above Room Temperature in Electron-Doped Hydride Compounds under High Pressure. *Phys. Rev. Lett.* **123**, 097001 (2019).
33. H. Xie *et al.*, Hydrogen Pentagraphenelike Structure Stabilized by Hafnium: A High-Temperature Conventional Superconductor. *Phys. Rev. Lett.* **125**, 217001 (2020).
34. S. Poncé, E. R. Margine, C. Verdi, F. Giustino, EPW: Electron-phonon coupling, transport and superconducting properties

- using maximally localized Wannier functions. *Comp. Phys. Commun.* **209**, 116-133 (2016).
35. M. I. Erements, A. P. Drozdov, P. P. Kong, H. Wang, Semimetallic molecular hydrogen at pressure above 350 GPa. *Nat. Phys.* **15**, 1246-1249 (2019).
 36. P. Loubeyre, F. Occelli, P. Dumas, Synchrotron infrared spectroscopic evidence of the probable transition to metal hydrogen. *Nature* **577**, 631-635 (2020).
 37. C. S. Zha, Z. Liu, R. J. Hemley, Synchrotron Infrared Measurements of Dense Hydrogen to 360 GPa. *Phys. Rev. Lett.* **108**, 146402 (2012).
 38. S. Lebegue *et al.*, Semimetallic dense hydrogen above 260 GPa. *Proc. Natl. Acad. Sci. U.S.A.* **109**, 9766-9769 (2012).
 39. W.-L. Yim, H. Shi, Y. Liang, R. J. Hemley, J. S. Tse, Band Gaps and Effective Oscillator Models for Solid Hydrogen and H₂O Ice at High Pressure. *Correlations in Condensed Matter Under Extreme Conditions*, Springer, Cham, 107-126 (2017).